Parity breaking in directional solidification: Numerics versus amplitude equations

Wouter-Jan Rappel*
Department of Physics, University of California, San Diego, La Jolla, California 92093
and Institute for Nonlinear Science, University of California, San Diego, La Jolla, California 92093

Hermann Riecke
Department of Engineering Sciences and Applied Mathematics, Northwestern University, Evanston, Illinois 60208
(Received 16 May 1991)

Motivated by recent experiments on the directional solidification of nematic liquid crystals, the standard solidification model is investigated in detail, numerically (by the boundary-integral method) as well as analytically (using amplitude equations). For the parameter values suitable for the experiments, both approaches yield a parity-breaking instability to traveling waves as well as a period-doubling bifurcation. Moreover, they agree with each other quantitatively not only in the immediate vicinity of the expansion point of the amplitude equations but over quite some range of parameters. The resulting phase diagram is in general accord with that obtained in the experiments. Since the amplitude equations describe the interaction of two modes with resonating wave numbers q and $2q$, this demonstrates that both experimentally observed transitions have the same origin: the 1:2-mode interaction. In addition, a third oscillatory instability observed experimentally can also be traced back to this interaction. Some questions concerning the direction of some bifurcations are, however, as yet unresolved. Possible causes for these discrepancies are indicated. For other parameter values the amplitude equations predict that no traveling waves will arise from this mode interaction.

PACS number(s): 64.70.Md, 47.20.Hw, 68.10.Jy, 47.20.Ky

I. INTRODUCTION

In recent years there has been a lot of interest in understanding spatial and spatiotemporal patterns from a general point of view. Particular progress has been made in patterns arising in quasi-one-dimensional systems. The best known systems of this kind are directional solidification [1,2], directional viscous fingering [3], eutectic solidification [4], Taylor vortex flow [5], and convection in a narrow channel [6]. Although these systems are very much constrained geometrically, they show a rich variety of patterns and transitions: spatially period-doubling instabilities, traveling waves, sources, sinks, and solitary modes. At the same time, despite the large differences in the microscopic equations, the phenomena are sufficiently similar in these systems that a unified description appears possible.

In one-dimensional systems the secondary bifurcations (those off the cellular pattern), can be classified by examining the different ways to break the symmetry of the pattern. For cellular patterns which are invariant under translations in space and time, and which are reflection symmetric, Coullet and Iooss [7] have shown that one can expect ten different secondary bifurcations. Not all of them have been observed yet.

In this paper we show that various transitions observed in the experiments can be understood to arise from the interaction of two relevant modes which have resonant wave numbers q and $2q$. We concentrate on the experiments by Libchaber and co-workers [1,2] on nematic liquid crystals where the transition between the isotropic and the nematic phase is utilized. In these experiments, similar to ordinary directional solidification, the material is pulled through a fixed temperature gradient with a pulling velocity v_0, resulting in a moving nematic-isotropic interface. Due to the diffusion of impurities the flat interface can become unstable to spatial modulations. For sufficiently small sample thickness spatially period-doubled states, traveling modes, and solitary modes are observed in these experiments. To model this system we use the standard directional-solidification model [8]. We investigate this model numerically using the boundary-integral method [9] and analytically within the framework of coupled amplitude equations describing the above-mentioned resonant mode interaction. Both approaches yield a parity-breaking bifurcation to traveling waves and an instability to a spatially period-doubled state. What is more, both approaches agree quantitatively with each other not only in the vicinity of the mode-interaction point but over quite some range of parameters. This confirms the above interpretation of the origin of these phenomena.

As argued by Coullet, Goldstein, and Gunaratne [10] the solitary traveling modes observed in experiments can be described by a bifurcation which breaks the reflection symmetry of the original steady-state pattern, i.e., by a parity-breaking bifurcation which gives rise to traveling-wave states, if this bifurcation is subcritical. Then kinks connecting the reflection-symmetric with the asymmetric state can arise. Such kink-antikink pairs exhibit all the qualitative features of the experimentally discovered inclusion. In fact, an extension of the model [11] has been shown to mimic the collision of the inclusions. They did not show that such a bifurcation in fact occurs in these

systems. Our calculations show that the standard model does in fact exhibit a parity-breaking bifurcation. For all the parameter values investigated, it is, however, supercritical.

The paper is organized as follows: In Sec. II the experimental system is described and the equations used to describe it are discussed. In Sec. III, the equations are formulated as an integro-differential equation. Section IV describes the coupled amplitude equations and the bifurcations resulting from them. The calculations of the coefficients of the amplitude equations are given in the Appendix. Independently, these coefficients have also been calculated by Haug [12], who discussed reflection-symmetric solutions only. The numerical results are compared with those of the amplitude equations in Sec. V. Finally, we conclude with a discussion in Sec. VI.

II. BASIC EQUATIONS

In this section we review the experimental setup and the basic equations of directional solidification. The liquid crystal is placed between two conducting plates, with a small spacing between them. Although the spacing does have an effect on the experiment we assume that the system is two dimensional. The temperature is externally imposed and thus fixed. The bath is pulled with a certain pulling velocity v_0 towards the cold end. In Fig. 1 we have schematically drawn the experimental setup.

We assume that the alloy is characterized by the phase diagram in Fig. 2. In both the liquid and the solid phase (for the liquid-crystal case this is the nematic and isotropic phase) the concentration field obeys the diffusion equation

$$D_L \nabla^2 c = \frac{\partial c}{\partial t} \quad \text{(liquid)} ,$$

$$D_S \nabla^2 c = \frac{\partial c}{\partial t} \quad \text{(solid)} , \tag{1}$$

where D_L and D_S are the diffusion constants in the liquid and solid, respectively. The concentration far away from the interface, c_∞, is fixed for each experiment. Local thermodynamic equilibrium requires that the temperature is the same on both the liquid and the solid sides of the interface. From the phase diagram we have

$$T_S = \tilde{T}_M - c_S m_S ,$$

$$T_L = \tilde{T}_M - c_L m_L ,$$

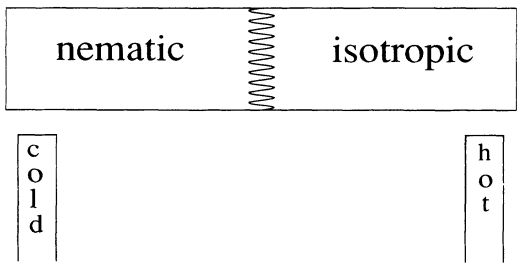

FIG. 1. Schematic setup of the experiment.

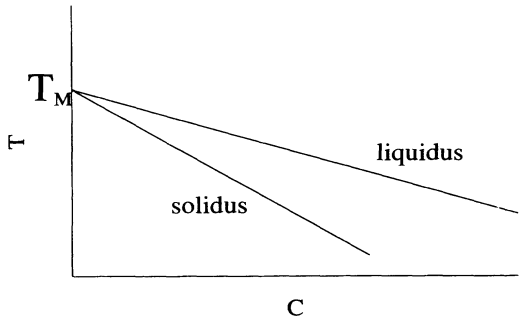

FIG. 2. Phase diagram of the alloy; temperature T vs concentration c.

where m_S (m_L) and c_S (c_L) are, respectively, the slope dT/dc in the solid (liquid) phase and the concentration on the solid (liquid) sides of the interface. Since $T_L = T_S$ the concentrations in the liquid and solid sides are related by the ratio of the liquidus and of the solidus: $c_L = c_S m_S / m_L$. $\tilde{T}_M$ is the melting temperature for the pure material ($c=0$) and has a Gibbs-Thomson shift due to the curvature κ: $\tilde{T}_M = T_M(1 - d_0\kappa)$, where the capillary length d_0 can be expressed in terms of the surface energy σ and the latent heat L: $d_0 = \sigma / L$.

The final boundary condition follows from the conservation of matter,

$$-v_n(c_L - c_S) = D_L(\hat{\mathbf{n}}\cdot\nabla c)_L - D_S(\hat{\mathbf{n}}\cdot\nabla c)_S , \tag{2}$$

where v_n is the normal velocity. In the case of a directional-solidification experiment the temperature is imposed externally. For convenience let us choose

$$T(y) = T_M + Gy , \tag{3}$$

so that at $y=0$ we have $T = T_M$. At the interface, we therefore have

$$c_L = -\frac{Gy}{m_L} - \frac{d_0\kappa}{m_L} . \tag{4}$$

To cast the equations in their final form we go to the moving frame, rescale c by c_∞ and rescale the lengths by the diffusion length $v_0/2D_L$ and time by $v_0^2/4D_L$. Then the equations read

$$\nabla^2 c + 2\frac{\partial c}{\partial y} = \partial_t c \quad \text{(liquid)} , \tag{5}$$

$$\alpha\nabla^2 c + 2\frac{\partial c}{\partial y} = \partial_t c \quad \text{(solid)} , \tag{6}$$

with boundary conditions at the interface,

$$(\hat{\mathbf{n}}\cdot\nabla c)_L - \alpha(\hat{\mathbf{n}}\cdot\nabla c)_S = -v_n(1-k)c_L\hat{n}_y , \tag{7}$$

$$c_L = \frac{c_S}{k} = \frac{-y}{\xi} - \gamma\kappa , \tag{8}$$

where $k = m_L/m_S$, $\alpha = D_S/D_L$, $\gamma = vd_0T_M/2D_L m_L c_\infty$, and $\xi - vm_L c_\infty/2D_L G$. The normal velocity v_n can be written as the sum of the constant translational velocity

in the y direction, which is 2 in the rescaled variables, and a possible contribution from the interface at $y=\zeta$:

$$\hat{n}_y v_n = 2 + \partial_t \zeta \ . \tag{9}$$

III. NUMERICAL APPROACH

The numerical approach consists of rewriting the above equations for the steady state (i.e., setting the right-hand side of (5) and (6) to zero) into an integro-differential equation over the unknown boundary, parametrizing this unknown boundary and finding the possible solutions. To derive the integro-differential equation let c_l be equal to c everywhere in the liquid and zero in the solid. Let c_s be the same with the solid and liquid reversed. From Eqs. (5)–(8) and the boundary condition $c \to 1$ at ∞, we can write

$$\begin{aligned} c_l &= 1 + \int c_L \hat{\mathbf{n}} \cdot \nabla G_L \, ds - \int G_L \phi_1 ds \ , \\ c_s &= \alpha \int c_S \hat{\mathbf{n}} \cdot \nabla G_S ds - \int G_S \phi_2 ds \ , \end{aligned} \tag{10}$$

where the integration is over the interface, ϕ_1 and ϕ_2 are unknown functions, and where G_L and G_S are the Green's functions for the liquid and the solid, respectively,

$$\begin{aligned} \nabla^2 G + 2\frac{\partial G}{\partial y} &= -\delta(\mathbf{x}-\mathbf{x}') \quad \text{liquid} \ , \\ \alpha \nabla^2 G + 2\frac{\partial G}{\partial y} &= -\delta(\mathbf{x}-\mathbf{x}') \quad \text{solid} \ . \end{aligned} \tag{11}$$

An important dimensionless parameter is the Péclet number p defined as $p = v\lambda/4D_L$. Then, for small Péclet numbers it is computationally efficient to use, as an explicit form of the Green's function,

$$G_L = \frac{1}{4p} e^{-(y-y'+|y-y'|)} + \frac{1}{2p} \sum_{n=1}^{\infty} \frac{\cos[n\pi(x-x')/p] e^{-\{y-y'+|y-y'|[1+(n\pi/p)^2]^{1/2}\}}}{[1+(n\pi/p)^2]^{1/2}} \ , \tag{12}$$

$$G_L = \frac{1}{4p} e^{-(y-y'+|y-y'|)/\alpha} + \frac{1}{2p} \sum_{n=1}^{\infty} \frac{\cos[n\pi(x-x')/p] e^{-\{(y-y')/\alpha+|y-y'|[1/\alpha^2+(n\pi/p)^2]^{1/2}\}}}{[1/\alpha^2+(n\pi/p)^2]^{1/2}} \ . \tag{13}$$

For high Péclet numbers it is more efficient to use for the Green's function the expression

$$G_L = \sum_n \frac{1}{2\pi} e^{-(y-y')} \times K_0(p[(x-x'+2n)^2+(y-y')^2]^{1/2}) \tag{14}$$

and a similar expression for G_S.

For the numerics we use the symmetric model, for which $\alpha=1$. Equations (10) reduce then to the single equation at the liquid interface

$$c_l = -\frac{y}{\xi} - \gamma\kappa = \int (1-k) \left[-\frac{y}{\xi} - \gamma\kappa \right] \hat{\mathbf{n}} \cdot \nabla G \, ds + 1 \ . \tag{15}$$

For the experiment at hand, $\alpha=0.526$. The amplitude equations will be discussed for arbitrary α. In particular, the coefficients appearing in the amplitude equations were calculated for arbitrary α.

The computational procedure consists of parametrizing the (unknown) boundary with N points of equal arclength separation. Since the cell is symmetric around the middle we can choose for our computational box just a box of size $\lambda/2$. As our independent variables we take the normal angle $\hat{\mathbf{n}} \cdot \hat{\mathbf{y}} = \cos\theta$ defined on the midpoints of the points of equal arclength. The additional independent variable is the position of the cell: y_0. The $N+1$ equations are the $N-1$ integral equations on the points of equal arclength except the interval end points and the requirement that the slope vanishes at both the tip and the tail. One has to be careful with possible divergences in the integral. A detailed account of this difficulty is given in Kessler and Levine [13].

The resulting $N+1$ nonlinear equations were iterated using Newton's algorithm. In our program we have used the CLAMS routine DNSQE with an absolute accuracy of 10^{-5}.

A question which should be addressed is for which N (number of discretization points) we get an accurate result. A discretization of ten points already gives a correct qualitative behavior. However, for accurate quantitative results it is necessary to discretize the interface by at least 50 points. In Fig. 3 we have plotted the wavelength at which a mixed solution bifurcates to a pure period-doubled state (this bifurcation will be discussed in great detail below). As we can see, the point of bifurcation converges for increasing number of discretization points. For all our calculations discussed below we have used 50 points.

As we have reported before [14], it is quite easy to find traveling-wave solutions with the above method. These modes have a nonzero transverse velocity v_x, in addition to the pulling velocity in the y direction. If we go into a frame which is moving with $\mathbf{v} = v_x \hat{\mathbf{x}} + v_0 \hat{\mathbf{y}}$ the mode is stationary again. Thus we modify Eqs. (5)–(8) for $\alpha=1$ to

$$\begin{aligned} &\nabla^2 c + \frac{2D_L}{v_y} \mathbf{v} \cdot \nabla c = 0 \quad \text{(liquid)} \ , \\ &\nabla^2 c + \frac{2D_L}{v_y} \mathbf{v} \cdot \nabla c = 0 \quad \text{(solid)} \ , \\ &(\hat{\mathbf{n}} \cdot \nabla c)_L - (\hat{\mathbf{n}} \cdot \nabla c)_S = -2(1-k) c_L \hat{n}_y \ , \\ &c_L = \frac{c_S}{k} = \frac{-y}{\xi} - \gamma\kappa \ . \end{aligned} \tag{16}$$

Equation (15) remains the same and the Green's function is modified to

$$G=\sum_n \frac{1}{2\pi} e^{-(y-y')-(v_x/2)(x-x'+2n)} K_0\left[\left[p^2+\frac{v_x^2}{4}\right]^{1/2}[(x-x'+2n)^2+(y-y')^2]^{1/2}\right] . \tag{17}$$

The cell does not have reflection symmetry around the midline of the cell and consequently we have to determine the shape of the total cell. As an extra variable we now have to determine v_x and the number of discretization points is 100.

Once we have found steady-state solutions we can examine their stability. For this we will use the quasistatic approximation, i.e., we neglect the time derivative of the concentration field but allow the interface to have a nonconstant normal velocity. Details of this approach can be found in Kessler and Levine [15]. In brief, Eq. (15) is thus modified to

$$c_l=-\frac{y}{\xi}-\gamma\kappa=\int(1-k)\left[-\frac{y}{\xi}-\gamma\kappa\right]\hat{\mathbf{n}}\cdot\nabla G\,ds+\int(1-k)\left[-\frac{y}{\xi}-\gamma\kappa\right]G\partial_t\zeta\,ds+1 . \tag{18}$$

The basic idea is to perturb the steady-state solution with a small normal shift, substitute this perturbation into the integro-differential equation above, linearize and solve the resulting eigenvalue problem for the growth rate of the perturbation.

To be more specific, we perturb by

$$\mathbf{x}(s)=\mathbf{x}_0(s)+\hat{\mathbf{n}}_0(s)\delta(s,t) , \tag{19}$$

where we assume that $\delta(s,t)=\delta(s)e^{\mu_1 t}$ and $\delta(s)\ll 1$. We substitute this perturbation into (18) and linearize in δ. This gives us the rather messy looking equation

$$\begin{aligned}\int ds'\Bigg[&(1-k)\left[\frac{y_0}{\xi}+\gamma\kappa_0\right][\delta(s')\hat{\mathbf{n}}_0'\cdot\nabla'+\delta(s)\hat{\mathbf{n}}_0\cdot\nabla]\hat{\mathbf{n}}_0'\cdot\nabla' G+(1-k)\left[\frac{\delta(s')}{\xi}-\gamma[\delta''(s')+\kappa_0^2\delta(s')]\right]\hat{\mathbf{n}}_0'\cdot\nabla' G\\&+(1-k)\left[\frac{y_0}{\xi}+\gamma\kappa_0\right][-\delta'(s')\hat{\mathbf{t}}_0'\cdot\nabla' G+\kappa_0\delta(s')\hat{\mathbf{n}}_0'\cdot\nabla' G]\Bigg]+\left[\frac{\delta(s)}{\xi}-\gamma[\delta''(s)+\kappa_0^2\delta(s)]\right]\\&=-\mu_1\int ds'(1-k)\left[\frac{y_0}{\xi}+\gamma\kappa_0\right]\delta(s')G ,\end{aligned} \tag{20}$$

where $\hat{\mathbf{t}}_0$ is the tangent vector of the steady-state solution.

Once we have chosen M points with equal arclength ds, the discretization of the integrals gives us a set of equations of the form

$$\sum_{j=0}^{M} A_{ij}\delta_j=\mu_1\sum_{j=0}^{M} B_{ij}\delta_j . \tag{21}$$

This is just an ordinary eigenvalue problem for μ_1 and can be solved with one of the standard numerical packages.

We can either perturb the steady state by a perturbation which is symmetric with respect to the end points of our computational box or one which is antisymmetric. The latter corresponds to a parity-breaking perturbation and we expect that at the point where the traveling-wave branch merges with the steady-state branch, the stability of this steady-state mode will change. As we have reported before [14], this is indeed the case.

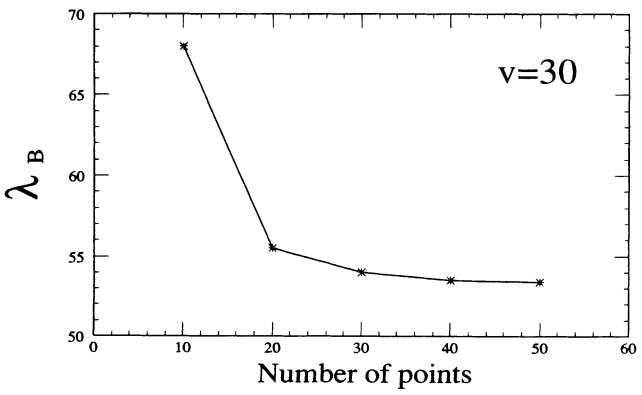

FIG. 3. The wavelength at which the mixed mode S_+ merges with the period-doubled mode S_2 as a function of the number of discretization points (these modes are discussed in detail in Sec. IV).

IV. AMPLITUDE EQUATIONS

Let us now return to the basic equations (5)–(8). To derive the amplitude equations it is useful to introduce the fields

$$u(x,y,t)=c_l(x,y,t),\quad y>\zeta \tag{22a}$$

$$w(x,y,t)=c_s(x,y,t),\quad y<\zeta \tag{22b}$$

and the interface position $\zeta(x,t)$. Equations (5) and (6) can then be rewritten as

$$\partial_x^2 u+\partial_y^2 u+2\partial_y u=\partial_t u , \tag{23a}$$

$$\partial_x^2 w+\partial_y^2 w+2\alpha^{-1}\partial_y w=\alpha^{-1}\partial_t w \ , \tag{23b}$$

and the boundary conditions at $y=\zeta(x,t)$ read

$$-\partial_x\zeta(\partial_x u-\alpha\partial_x w)+\partial_y u-\alpha\partial_y w = -(2+\partial_t\zeta)u(1-k) \ , \tag{24}$$

$$u=-\frac{\zeta}{\xi}+\gamma\frac{\partial_x^2\zeta}{[1+(\partial_x\zeta)^2]^{3/2}} \ , \tag{25}$$

$$w=ku \ . \tag{26}$$

These equations have a trivial planar solution,

$$u_0(y)=1+\left[\frac{1}{k}-1\right]e^{[-2(y-\zeta_0)]} \ ,$$
$$w_0=1 \ , \tag{27}$$
$$\zeta_0=-\xi/k \ ,$$

with interface position $\zeta=\zeta_0$. When we increase the pulling velocity above a certain critical velocity this planar interface becomes unstable due to the well-known Mullins-Sekerka instability [8]. To get the dispersion relation, we perturb the planar base solution with a sinusoidal perturbation with growth rate μ_1,

$$u=u_0+\eta u_1 e^{iqx+\lambda_1 y+\mu_1 t} \ , \tag{28a}$$

$$w=1+\eta w_1 e^{iqx+\Lambda_1 y+\mu_1 t} \ , \tag{28b}$$

$$\zeta=\zeta_0+\eta\zeta_1 e^{iqx}e^{\mu_1 t} \ , \tag{28c}$$

where $\lambda_1^2+2\lambda_1-q^2=0$ and $\Lambda_1^2+(2/\alpha)\Lambda_1-q^2=0$. Before substituting these expressions into the boundary conditions (24)–(26) one has to take into account that they apply at $y=\zeta(x,t)$ with $\zeta(x,t)$ given by (28c). This is done by expanding u and w at the interface $y=\zeta(x,t)$ around $y=\zeta_0$. Substituting these expressions into the boundary conditions and linearizing in η we get an equation for μ_1 [cf. (A6) in the Appendix]. The neutral curve is defined as the curve in parameter space at which $\mu_1=0$. In the velocity–wave-number space the neutral stability curve (v,q) is closed as shown in Fig. 4. Inside the curve the planar interface is unstable to perturbations with the respective wave numbers.

TABLE I. Parameter values of the liquid-crystal system used in the numerical calculation.

Parameter	Value
d_0	2×10^{-8} cm
G	23.3 K/cm
T_M	313.65 K
m_l	1°/mol %
c_∞	1.2 mol %
D_l	3.8×10^{-6} cm/s^2
D_s	3.8×10^{-6} cm/s^2
k	0.88

To describe the nonlinear evolution of these perturbations we derive amplitude equations for the modes in question. The details of this derivation will be given in the appendix. Here we concentrate on the general aspects of the results. At the minimum (v_c,q_c) of the neutral curve there is only a single such mode. Denoting the amplitude of the corresponding interface deflection by Z_1, i.e., $\zeta(x,t)=\zeta_0+Z_1(t)e^{iq_c x}+\text{c.c.}+\ldots$, (the ellipsis denotes higher-order terms) one obtains the following Landau equation:

$$\dot{Z}_1=\mu_1 Z_1+g|Z_1|^2 Z_1 \ . \tag{29}$$

Since the system has translation symmetry, $x\to x+\Delta x$, the amplitude equation has to be invariant under $Z_1\to Z_1 e^{iq_c\Delta x}$. The lowest-order term is therefore cubic. The sign of the cubic coefficient g determines the nature of the bifurcation. If $g<0$ we have a supercritical or forward bifurcation while if $g>0$ we have subcritical or backward bifurcation. The value of g has been calculated first by Caroli, Caroli, and Roulet [17] for arbitrary values of α. Although they obtained the right sign, a small error in their calculation was corrected by Wollkind, Oulton, and Sriranganthan [18]. We have calculated the value of g for the parameter values shown in Table I which characterize the liquid-crystal system. Figure 5

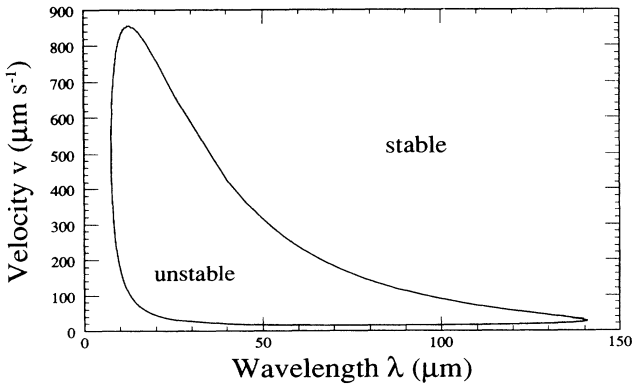

FIG. 4. The neutral stability curve in the parameter space (wavelength λ vs velocity v) for the material parameters in Table I. The planar interface is unstable inside the curve.

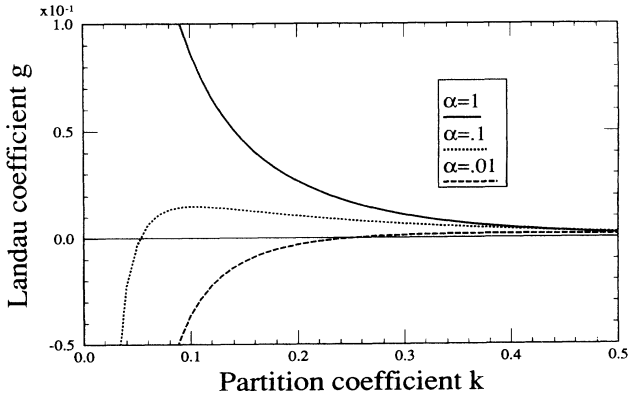

FIG. 5. The Landau coefficient g as a function of the partition coefficient k for various values of α.

gives g as a function of k for various values of α. It shows that for sufficiently small k the bifurcation can become subcritical, as is usually the case in the solidification of metals [19]. The tricritical line ($g=0$) in α-k space is shown in Fig. 6.

Above the minimum more perturbation modes become relevant. In particular, for the case of an infinite system a continuum of modes arises. This can be taken into account by allowing slow spatial variations in the amplitude Z_1, leading to a Ginzburg-Landau equation. In the present paper we will not discuss this in detail. Instead we will focus on another aspect arising from the widening of the neutral curve.

A characteristic feature of directional solidification is the fact that the neutral curve is very flat (see Fig. 4). This implies that rather close to its minimum it is already wide enough that perturbation modes with *resonating* wave numbers q and $2q$ become relevant [20]. Previous analyses in other systems have shown that such resonances can have a strong influence on the dynamics. In particular, in Taylor vortex flow it has been shown that this resonance modifies the band of Eckhaus-stable wave numbers considerably [21] and can lead to a new instability which limits the wave-number band but is not of the long-wavelength Eckhaus type [22]. It is important to note that the effects of such resonances cannot be described by a single-mode Ginzburg-Landau equation. Since the neutral curve of the present system is flatter than that of Taylor vortex flow, it is to be expected that these resonance effects are even more pronounced. In the following we therefore investigate the amplitude equations pertaining for the dominant resonance.

The appropriate starting point is the point in parameter space where both the mode with wave number q and that with wave number $2q$ go unstable simultaneously. In the vicinity of this codimension-2 point the interface deflection has to be expanded in both modes, $\zeta(t)=\zeta_0+Z_1(t)e^{iqx}+Z_2(t)e^{2iqx}+\text{c.c.}+\ldots$ (the ellipsis denotes higher-order terms), and one obtains the coupled amplitude equations

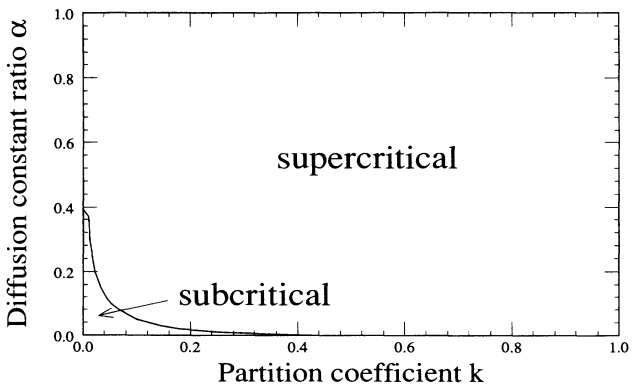

FIG. 6. The tricritical line, $g=0$. To the left of the line the Landau coefficient g is negative and the bifurcation off the planar interface is subcritical, while to the right g is positive and the bifurcation is supercritical.

$$\dot{Z}_1=\mu_1 Z_1+c_1 Z_1^* Z_2+a_1 Z_1|Z_1|^2+b_1 Z_1|Z_2|^2 , \tag{30a}$$

$$\dot{Z}_2=\mu_2 Z_2+c_2 Z_1^2+b_2 Z_2|Z_1|^2+a_2 Z_2|Z_2|^2 . \tag{30b}$$

The form of these equations is again already determined by the fact that they have to be equivariant under $Z_1\to Z_1 e^{iq\Delta x}$, $Z_2\to Z_2 e^{2iq\Delta x}$ (translation symmetry), and under $Z_1\to Z_1^*$, $Z_2\to Z_2^*$ (reflection symmetry). The latter assures that the coefficients are real. Calculating the coefficients from the basic equations (23)–(26) involves a considerable amount of algebra which is discussed in the Appendix.

The amplitude equations (30) have been studied previously by various authors [23-25]. Here we summarize their main results and plot a typical bifurcation diagram arising from these analyses. We will follow the analysis of Proctor and Jones [23].

We use the translational invariance of the problem and write

$$Z_1=\rho e^{i(\psi+\chi)/4},\quad Z_2=\sigma e^{i(\psi-\chi)/2} , \tag{31}$$

introducing the spatial phase ψ and the temporal phase χ. Since ψ is not invariant under translations it cannot enter the dynamical equations. Substituting this into (30), and equating real and imaginary parts, one obtains a set of three coupled equations for ρ, σ, and χ,

$$\dot{\rho}=\mu_1\rho+c_1\rho\sigma\cos\chi+a_1\rho^3+b_1\rho\sigma^2 , \tag{32a}$$

$$\dot{\sigma}=\mu_2\sigma+c_2\rho^2\cos\chi+a_2\sigma^3+b_2\sigma\rho^2 , \tag{32b}$$

$$\dot{\chi}=-(c_2\rho^2/\sigma+2c_1\sigma)\sin\chi , \tag{32c}$$

and a separate equation for ψ,

$$\dot{\psi}=(c_2\rho^2/\sigma-2c_1\sigma)\sin\chi . \tag{33}$$

There are three different types of steady-state solutions of Eqs. (32) (i.e., with $\dot{\rho}=\dot{\sigma}=\dot{\chi}=0$).

(i) Pure modes, which we will call S_2:

$$\rho=0,\quad \sigma^2=\frac{-\mu_2}{a_2},\quad \chi_-=0,\quad \chi_+=\pi . \tag{34}$$

These solutions represent cells with wave number $2q$ and the coefficient a_2 is the corresponding Landau coefficient g. They exist if $\mu_2 a_2<0$ and lose their stability to mixed modes when the inequality

$$\mu_1<\frac{b_1\mu_2}{a_2}\pm c_1\left[\frac{-\mu_2}{a_2}\right]^{1/2} \tag{35}$$

is violated. The phase χ does not play a role for this mode but it will for the remaining two steady-state modes.

(ii) Mixed modes, denoted by $S_\pm$:

$$0=\mu_1\pm c_1\sigma+a_1\rho^2+b_1\sigma^2 ,$$

$$0=\mu_2\sigma\pm c_2\rho^2+a_2\sigma^3+b_2\sigma\rho^2 , \tag{36}$$

$$\chi_-=0,\quad \chi_+=\pi .$$

The two mixed modes represent cells with wave number q which have a nonzero amplitude in their first harmonic

$2q$. The mixed mode S_- undergoes a Hopf bifurcation on the line given by (36) together with

$$a_1\rho^2+a_2\sigma^2=\frac{c_2\rho^2}{2\sigma} , \tag{37}$$

which gives rise to standing waves characterized by $\dot{\chi}=0=\dot{\psi}$, but time-dependent amplitudes ρ and σ.

(iii) Traveling waves, denoted by TW:

$$\rho^2=-2\frac{c_1}{c_2}\sigma^2, \quad \sigma^2=\frac{2\mu_1+\mu_2}{\Delta} , \tag{38}$$

$$\cos\chi=\frac{\mu_2[2(c_1/c_2)a_1-b_1]+\mu_1[-2(c_1/c_2)b_2+a_2]}{c_1\sigma\Delta} , \tag{39}$$

with

$$\Delta\equiv 4\frac{c_1}{c_2}a_1-2b_1+2\frac{c_1}{c_2}b_2-a_2 . \tag{40}$$

These traveling waves exist provided that $c_1/c_2<0$ and $|\cos\chi|\le 1$, i.e.,

$$\left[\mu_2\left[2\frac{c_1}{c_2}a_1-b_1\right]+\mu_1\left[-2\frac{c_1}{c_2}b_2+a_2\right]\right]^2 \le c_1^2(2\mu_1+\mu_2)\Delta , \tag{41}$$

and bifurcate off $S_\pm$ at $|\cos\chi|=1$. Within the amplitude equations (30) this bifurcation is always supercritical. Note that the fifth-order terms invoked in Ref. [2] are in fact not necessary for the occurrence of traveling waves. The TW's can become unstable to modulated waves (MW's) with time-dependent amplitudes and phases. In addition, for certain parameter ranges a homoclinic orbit arises which is structurally stable due to the symmetry of the system [23,25].

As an example of a phase diagram arising from the analysis above, the bifurcation lines corresponding to the liquid-crystal experiment are plotted in Fig. 7 as functions of μ_1 and μ_2, which in turn depend on v and q [cf. (A6) and (A7) in the Appendix]. The solid line denotes the bifurcation of the mixed modes $S_\pm$ off the pure mode S_2, given by (35). At the dotted curve the mixed mode S_- loses its stability against the standing wave [given by (36) with (37)]. To the right of the dashed curve condition (41) for the existence of the traveling wave is satisfied. For these lines the coefficients a_i, b_i, and c_i have been evaluated not at the codimension-2 point ($\mu_1=0=\mu_2$), but at the parameter values in question [$\mu_i=\mu_i(q,v)$]. This takes certain higher-order corrections into account (see the Appendix) which considerably improve the agreement with the numerical result (cf. Fig. 12). For comparison, the corresponding results with the coefficients evaluated at $\mu_1=0=\mu_2$ are shown as thin lines.

V. COMPARISON BETWEEN THE AMPLITUDE EQUATIONS AND THE NUMERICAL RESULTS

Before comparing the numerical results with those of the coupled amplitude equations it is useful to check the numerical resolution using the neutral stability curve and the single-mode amplitude equation (29). Figure 8 shows the results for the neutral curve around the codimension-2 point. Here the solid curves are given by the dispersion relation [Eq. (A6) below] and the asterisks denote the location where the numerically determined cellular solution becomes planar. For the discretization chosen in all of the subsequent calculations (50 points in a computational box) the neutral stability curve corresponding to the q mode agrees very well with (A6) while the one corresponding to the $2q$ is shifted upwards a little bit. This is due to the fact that for the $2q$ curve the effective resolution is only half as fine since a *full* cell rather than half a cell is contained in the computational box.

Near the minimum (v_m,q_m) of the neutral stability curve only one mode goes unstable. In Fig. 9 the numerically determined amplitude of the cell at the critical wave number is plotted as a function of the velocity v. The figure shows that the bifurcation from the planar to a cellular interface is supercritical (or forward) not only for $k=0.88$ but also for $k=0.4$ (inset). In fact, the nonlinear

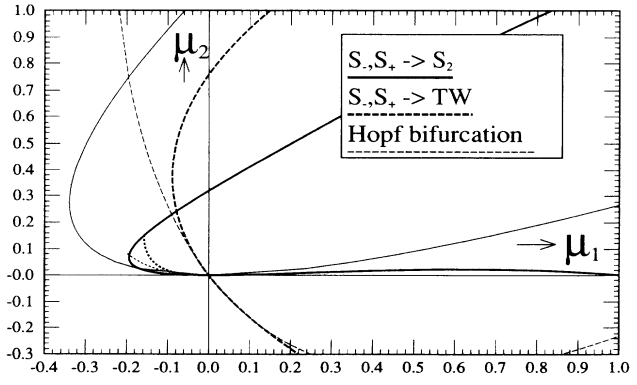

FIG. 7. The set of bifurcation lines as derived from the coupled amplitude equations for the liquid-crystal experiment. For an explanation see the text.

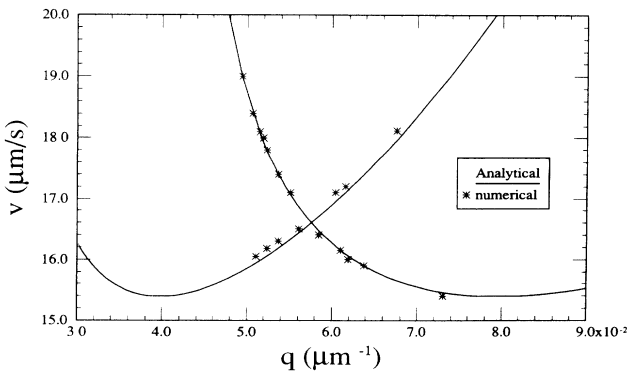

FIG. 8. The numerical and analytical results for the neutral curves in the vicinity of the codimension-2 point ($q_c=0.057$, $v_c=16.59$).

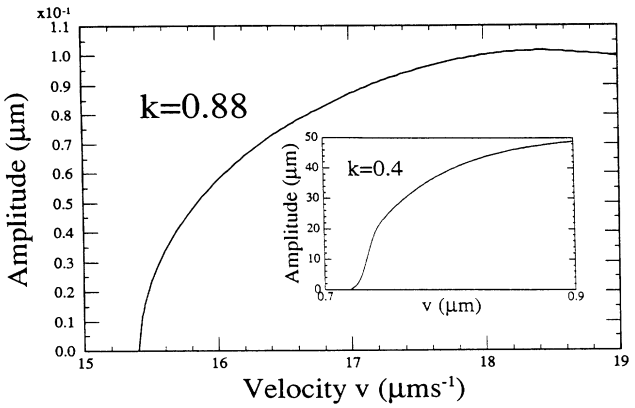

FIG. 9. The amplitude of the cell at the minimum of the neutral stability curve for $k=0.88$. The inset shows the same plot but now for $k=0.4$.

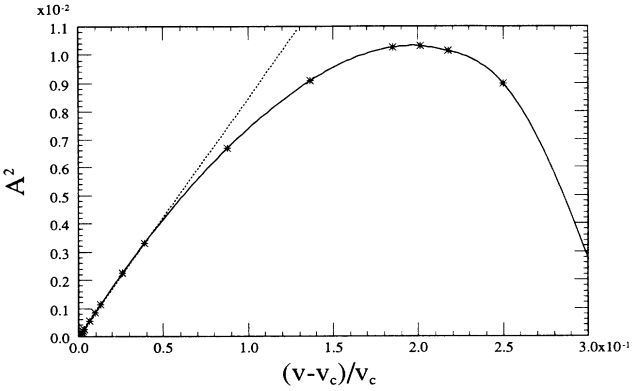

FIG. 10. The square of the amplitude of the cell at the minimum of the neutral stability curve ($k=0.88$) as a function of $v-v_c/v_c$. The dashed line is the approximate slope at $v=v_c$ (see text).

analysis of Sec. IV shows that for $\alpha=1$ (i.e., in the symmetric model) the bifurcation is supercritical for all values of k (see Table II). In fact, we can perform an expansion similar to that performed by Caroli, Caroli, and Roulet [17], who show that in the one-sided model ($\alpha=0$) the bifurcation becomes subcritical for $k<0.45$ (see also Fig. 6). The same expansion for the symmetric model shows that the bifurcation is always supercritical [26].

More quantitatively, close to threshold the amplitude A of the cells scales as

$$A^2=\frac{d\mu_1}{dv}\frac{v-v_c}{v_c}\frac{v_c}{g}\ , \tag{42}$$

where v_c is the critical velocity at which the planar interface becomes unstable. Using the analytical expressions for $d\mu_1/dv$ and v_c we can determine the value of g from the numerical calculation. In Fig. 10 A^2 is plotted versus $(v-v_c)/v_c$ for $k=0.88$ with $v_c=15.4$ μm and $d\mu_1/dv=0.28$. The slope turns out to be 0.092 which yields a Landau coefficient $g=-48$. This agrees very well with the value found in Sec. IV and Table II ($g=-50$).

We now present the results of our numerical calculations. As mentioned before, we can find all the steady-state solutions and can therefore determine where in parameter space certain bifurcations occur. Indeed, we have found mixed mode solutions (S_+,S_-), pure mode solutions (S_2), and traveling waves (TW). Typical examples of these modes are given in Figs. 11(a) and 11(b).

The phase diagram shown in Fig. 12 summarizes the numerical results. The thin solid curves are the neutral stability curves for the q and the $2q$ mode. The bifurcations off the steady-state solutions to other steady-state

TABLE II. The Landau coefficient g for different values of k.

k	g
0.9	−27.8
0.88	−50
0.8	−238.7
0.7	−846.3
0.6	−2 273
0.5	−5 476
0.4	−12 346
0.3	−28 466
0.2	−71 267
0.1	−230 152

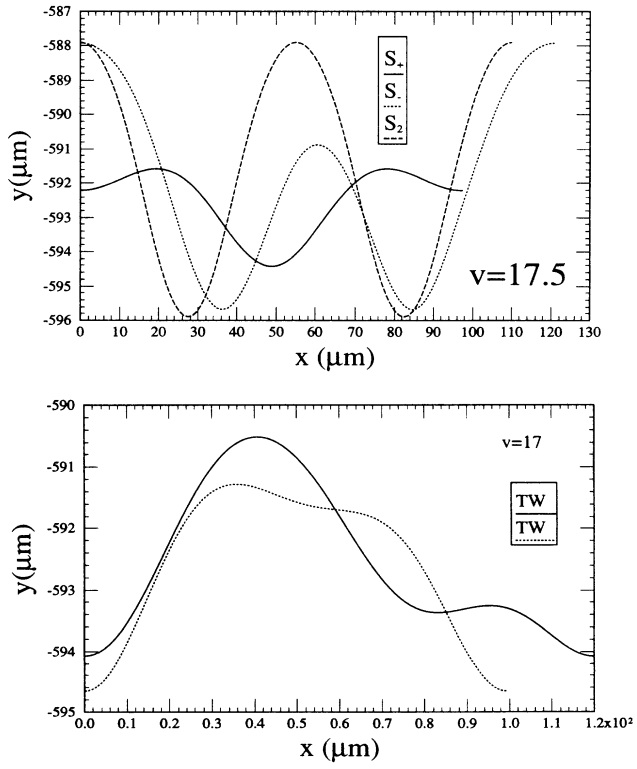

FIG. 11. (a) Typical shapes of the mixed modes S_+ and S_- and of the period-doubled cell S_2. (b) Typical shapes of the traveling-wave modes for two different wave numbers.

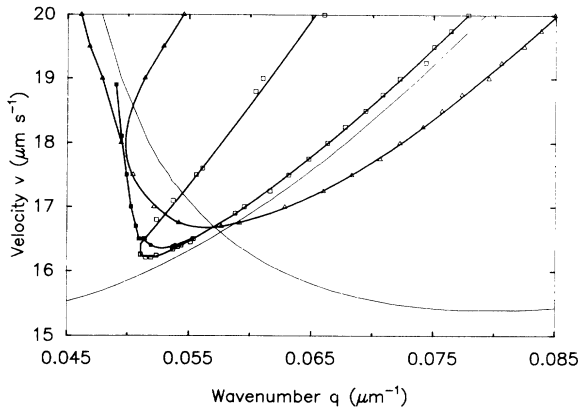

FIG. 12. The phase diagram showing the numerically determined bifurcations. The thin solid lines denote the (analytical) neutral stability curves for the q and $2q$ mode. The open boxes represent the bifurcation from the S_+ mode to the S_2 mode (to the right of the codimension-2 point), and from the S_- mode to the S_2 mode (the remaining part of the curve). The open triangles represent the bifurcation from the S_+ mode to the TW (to the right of the codimension-2 point) and from the S_- mode to the TW (to the left of the codimension-2 point). The solid circles represent the Hopf bifurcation of the S_- mode. The solid boxes are the positions of the saddle-node bifurcation of the S_- branch and the solid triangles are the positions of the saddle-node bifurcation of the TW branch (thick lines serve only as a guide to the eye).

solutions are represented by thick lines. In the following we describe them by taking cuts through the phase diagram at constant velocity. When comparing Fig. 12 with Fig. 7 one has to note that the axes $\mu_1=0$ and $\mu_2=0$ in Fig. 7 correspond to the neutral curves in Fig. 12. Thus Fig. 7 is rotated as compared to Fig. 12.

Figure 13 shows the amplitude of the $2q$ mode, Z_2, as we cut across the phase diagram at $v=16.5$ μm s^{-1}.

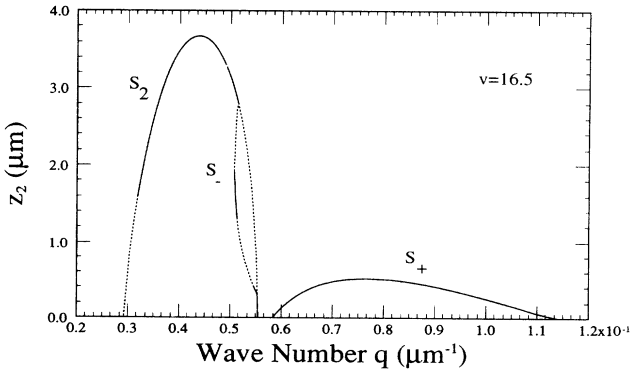

FIG. 13. The bifurcation diagram for a cut through Fig. 12 at $v=16.5$. Stable branches are denoted by solid lines, unstable by dotted lines, and branches with an undetermined stability by a dashed line (in Figs. 14 and 15). One stable regime of S_- is limited by the saddle-node bifurcation and a Hopf bifurcation, whereas the other regime is limited by a second Hopf bifurcation and the merging with S_2.

Note that this is below the codimension-2 point. Stable solutions are indicated by solid lines, unstable solutions by a dotted line, and solutions with an undetermined stability by dashed lines (in Figs. 14 and 15). We see that as we go from right to left (high q to low q) we first encounter the S_+ solution. This solution is stable for the whole branch. The branch vanishes when it hits the neutral stability curve. Then, as we cross the neutral stability curve for the $2q$ mode, the S_2 mode comes up. This pure mode loses its stability against the mixed mode S_- on the line connecting the open boxes in Fig. 12. Very close to this point S_- undergoes a Hopf bifurcation, which presumably leads to standing waves. It regains stability at a second Hopf bifurcation. The Hopf bifurcations are represented by solid circles in Fig. 12. After losing stability at a saddle-node bifurcation it merges again with the pure mode, again on the line connecting the open boxes. The S_2 mode regains its stability. There is no traveling-wave branch for this case, which is consistent with the stability of the S_+ branch. Note that the period-doubled solution S_2 loses its stability at small q, which can be attributed to the higher q modes.

For a slightly larger velocity ($v=17.5$ μm s^{-1}), the bifurcation diagram is shown in Fig. 14. Again, upon decreasing q the S_+ branch comes up, but now loses its stability to the traveling-wave branch TW (line connecting open triangles). This instability breaks the reflection symmetry (parity). The (unstable) S_+ branch continues until it merges with the S_2 branch on the line connecting the open boxes. The S_- branch starts at the neutral stability curve for the q mode, where it is still unstable, undergoes a saddle-node bifurcation (solid boxes in Fig. 12) and merges with the S_2 branch (open boxes in Fig. 12). The TW branch connects the S_+ branch with the S_- branch. It merges with the S_- branch at the line connecting the open triangles. We have not calculated the stability of the TW branch. Since it bifurcates off the stable mixed mode S_+ we expect it to be stable close to the bifurcation point. It is possible, however, that it subsequently undergoes a Hopf bifurcation to modulated waves [25].

At yet higher velocity, $v=19$ μm s^{-1}, we have the bifurcation diagram as in Fig. 15. There is no saddle-node bifurcation anymore in the S_- branch, but there is a new

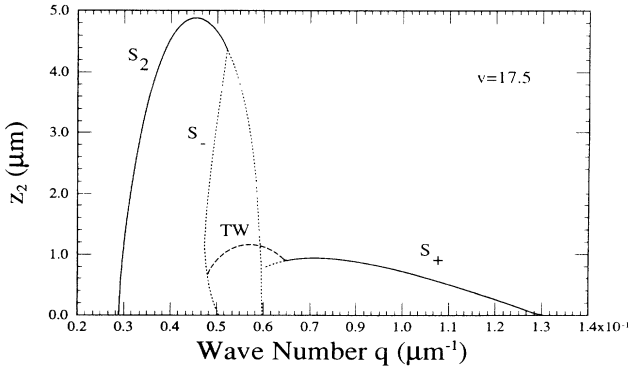

FIG. 14. As Fig. 13 but now for $v=17.5$.

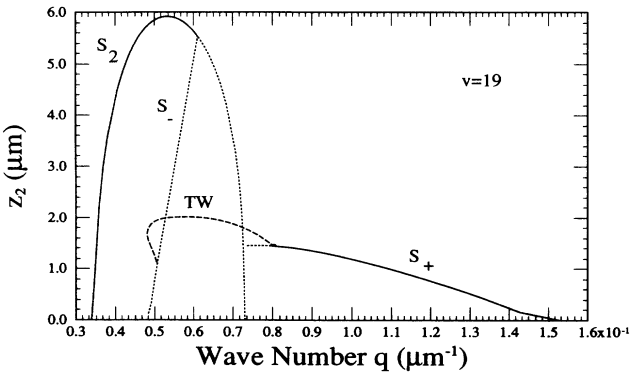

FIG. 15. As Fig. 13 but now for $v=19$.

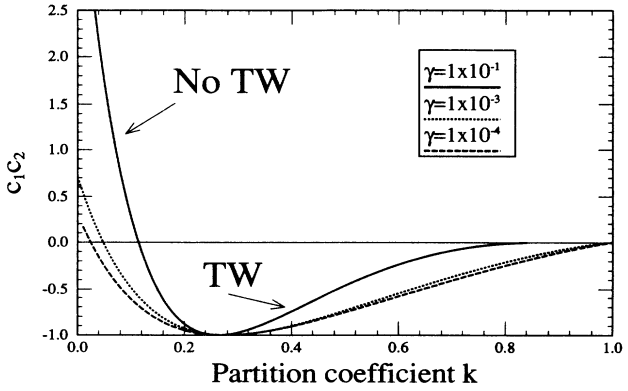

FIG. 17. The value of c_1c_2 for different values of γ as a function of k (for $\alpha=1$) at the codimension-2 point.

one in the TW branch. This saddle-node bifurcation is denoted by the line connecting the solid triangles in Fig. 12.

As discussed in Sec. IV, the coupled amplitude equations (30) describe this system in the vicinity of the codimension-2 point. In Fig. 16 these analytical results are compared with those obtained in the numerics. There the numerical phase diagram of Fig. 12 is redrawn omitting the lines connecting the symbols, i.e., S_+ and S_- merge with S_2 along the open boxes, the TW's bifurcate off S_+ (and S_-) along the triangles. The thick lines give the corresponding bifurcation lines as obtained from (30). For this comparison we have evaluated the coefficients a_i, b_i, and c_i not at the codimension-2 point but at the parameter values (v,q) in question. As expected, the agreement is very good close to the codimension-2 point (note again that for our numerical resolution the numerical neutral curve for the $2q$ mode is shifted to slightly higher values of v). More remarkably, the agreement continues to be good farther away. Thus the amplitude equations

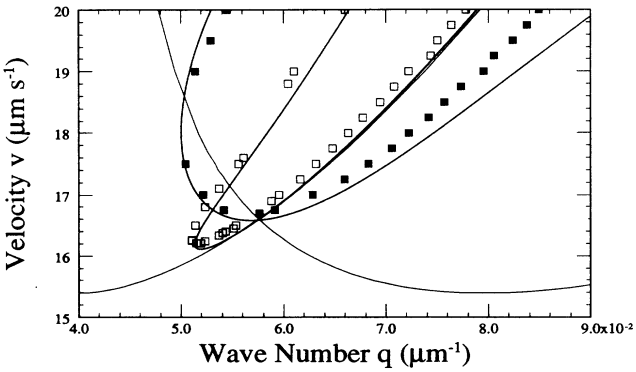

FIG. 16. Comparison of numerically and analytically obtained phase diagram. The solid boxes represent the bifurcation from the mixed modes to the pure period-doubled mode, while the open boxes represent the bifurcation from the mixed modes to the traveling-wave mode. The thick lines show the respective results of the amplitude equations (30). The thin lines give the neutral stability curves.

even capture the strong bend in the line along which the mixed mode S_- merges with S_2. This is not the case if the coefficients are evaluated at the codimension-2 point (cf. Fig. 12). The agreement shows clearly that both the traveling wave and the period-doubled states found in the numerics as well as in the experiments are due to the mode interaction $q-2q$. For the comparison with experiments it is important to note that in the full system the S_+ mode at a wave number q can be identified with the S_2 mode at a wave number $q/2$, since the latter contains two equal cells of wavelength $2\pi/q$. Therefore the bifurcation of S_- off S_2 at q_D, say, will also be found for the S_+ mode at $2q_D$. Since the commonly observed cellular state corresponds to the S_+ mode, it undergoes a spatial period-doubling bifurcation for values of large q. This has been observed experimentally [1].

The TW branch exists provided that $c_1c_2<0$ (see Sec. IV). It is therefore interesting to know whether there is a region in parameter space where this condition is not met and, consequently, there are no traveling waves. The basic equations have five independent parameters. The codimension-2 point fixes two of them, leaving a three-dimensional parameter space (k,γ,α). Rather than searching this space systematically we have taken some cuts through this space for constant α. In Fig. 17 the value of c_1c_2 is shown for the case $\alpha=1$ as a function of k for various values of γ. In fact, for sufficiently small k the product crosses zero and becomes positive. For these values of the parameters, no traveling waves arise from the mode interaction. Indeed, experiments on systems with small values of k do not exhibit traveling waves.

VI. DISCUSSION AND CONCLUSION

Motivated by recent directional-solidification experiments in nematic liquid crystals we have investigated the standard solidification model numerically as well as analytically. In both approaches we find a parity-breaking bifurcation to traveling waves and a period-doubling bifurcation in space. The analytical calculation is based on the interaction of modes with wave numbers q and $2q$. These calculations agree quantitatively with each other. In fact, they do so over quite some range of pa-

rameter values. This shows clearly that this mode interaction lies at the origin of both bifurcations and thus also explains the experimentally observed transitions to traveling inclusions and period-doubled states [1]. In addition, we find a Hopf bifurcation to (presumably) unstable standing waves, which may explain similar amplitude oscillations arising in the experiments [1]. Thus the phase diagram which we put forward in a previous publication [16] is confirmed, and seemingly unrelated transitions are found to be due to the same origin.

There are still some questions which need to be resolved. The present analysis does not address the stability of any of the solutions in large-aspect ratio systems, i.e., with respect to long-wavelength perturbations. Such perturbations could destabilize the S_+ mode before the bifurcations of interest are reached. In fact, close to the codimension-2 point this is to be expected, since the Eckhaus instability usually destabilizes the patterns well before the neutral curve— and therefore also before the codimension-2 point—is reached. Farther away, however, this need not be the case. In fact, in Taylor vortex flow the corresponding period-doubling bifurcation is reached stably for sufficiently large Reynolds numbers [22]. This question of stability can be addressed within the present solidification model.

The present understanding of the experiments [1,2] requires both the parity-breaking and the period-doubling bifurcation to be subcritical in order to account for the localized inclusions and the (apparent) stability of the period-doubled state, respectively. The present calculation shows that both of them are, however, supercritical for all parameter values considered. This suggests that additional physical phenomena have to be taken into account [27]. Whereas the experiments are performed in very thin layers with strong three-dimensional effects, the present model assumes a perfectly two-dimensional situation. The three-dimensional effects, the present model assumes a perfectly two-dimensional situation. The three-dimensional nature of the experiments will not only induce a meniscus but also lead to effects which are specifically due to the physics of the liquid crystal and would require a significant extension of the present model. Since the thickness is known to have a strong influence on the observed phenomena, this may well be the main reason for the discrepancies.

Note added. Meanwhile it has become clear that localized, stable traveling-wave inclusions can also be obtained even if the parity-breaking bifurcation is supercritical [28], as it was found in the present investigation. Thus the standard solidification model used here describes this transition adequately even in the liquid-crystal experiments.

ACKNOWLEDGMENTS

We would like to thank Herbert Levine for valuable discussions. W.-J. R. was supported by DARPA Grant No. N00011-86-K-0758. H. R. acknowledges support from the Aspen Center for Physics.

APPENDIX: CALCULATION OF THE COEFFICIENTS

Here the coefficients for the coupled amplitude equations (30) are calculated. A similar calculation has been performed independently by Haug [12]. We start from Eqs. (23)–(26) and expand the concentration field u as well as the interface position ζ,

$$u = u_0 + \cos qx\,[\eta u_{11} + \eta^2(u_{12y}y + u_{12}) + \eta^3(u_{13} + yu_{13y} + y^2u_{13yy})]e^{\lambda_1 y} + \cos 2qx\,[\eta u_{21} + \eta^2(u_{22y}y + u_{22}) + \eta^3(y^2u_{23yy} + yu_{23y} + u_{23})]e^{\lambda_2 y} + \eta^2 u_{42}\cos 4qx e^{\lambda_4 y} + \eta^2 u_{32}\cos 3qx e^{\lambda_3 y} + \eta^2 u_{02} e^{\lambda_0 y} + \cdots , \tag{A1}$$

$$\zeta = \zeta_0 + \cos qx\,(\eta z_{11} + \eta^2 z_{12} + \eta^3 z_{13}) + \cos 2qx\,(\eta z_{21} + \eta^2 z_{22} + \eta^3 z_{23}) + \cos 4qx\,(\eta^2 z_{42} + \eta^3 z_{43}) + \cos 3qx\,(\eta^2 z_{32} + \eta^3 z_{33}) + \eta^2 z_{02} + \eta^3 z_{03} + \cdots , \tag{A2}$$

with $\eta \ll 1$. The field w is expanded similarly with λ_i replaced by Λ_i. Note that for periodic boundary conditions (in x) one should allow complex amplitudes and expand in exponentials rather than a pure cosine series. Due to the reflection symmetry of the system, however, the coefficients in (30) are real and can easily be derived from those obtained in the present expansion, which involves less algebra [see (A16) below]. Thus, eventually no reflection symmetry is imposed on the solutions. We also expand the (control) parameters,

$$\xi = \frac{1}{\xi_0 + \eta\xi_1} , \tag{A3a}$$

$$\gamma = \gamma_0 + \eta\gamma_1 , \tag{A3b}$$

$$q = q_0 + \eta q_1 , \tag{A3c}$$

and introduce slow time scales $T_1 = \eta t$ and $T_2 = \eta^2 t$.

These expansions are now inserted into the diffusion equations (23) and the boundary conditions (24)–(26). Since the resulting algebra is very involved we used MACSYMA for these expansions and will only sketch the relevant steps [29]. At $O(\eta)$ the diffusion equations yield the decay lengths $\lambda_{1,2}$ and $\Lambda_{1,2}$,

$$\lambda_n = -1 - [1 + (nq_0)^2]^{1/2} , \tag{A4a}$$

$$\Lambda_n = -\alpha^{-1} + [\alpha^{-2} + (nq_0)^2]^{1/2} . \tag{A4b}$$

At higher order similar expressions will be obtained for $\lambda_{3,4}$ and $\mu_{3,4}$. The boundary conditions (25) and (26)

determine at this order u_{11}, u_{21}, v_{11}, and v_{21}. The remaining boundary condition (24) yields

$$\hat{\tau}_1 \partial_t z_{11} = \hat{\mu}_1 z_{11} \ , \tag{A5a}$$

$$\hat{\tau}_2 \partial_t z_{21} = \hat{\mu}_2 z_{21} \ , \tag{A5b}$$

with

$$\hat{\mu}_n = [\alpha k \Lambda_n - \lambda_n + 2(k-1)](\xi_0 + \gamma_0 n^2 q_0^2) - 2\frac{k-1}{k}(\lambda_n + 2) \ , \tag{A6}$$

$$\hat{\tau}_n = -(k-1)/k + \frac{-2(k-1)/k - \xi_0 - \gamma_0 n^2 q_0^2}{2\lambda_n + 1} + \frac{\xi_0 + \gamma_0 n^2 q_0^2 \alpha k}{2(\alpha \Lambda_n + 1)} \ . \tag{A7}$$

These equations determine the onset of the instability ($\hat{\mu}_i = 0$), since we require that the amplitudes do not depend on the fast time scale t. Writing the onset conditions in this (uncommon) way makes it easier to reconstitute the relevant amplitude equations later (see below) [30]. The codimension-2 point in question is given by the simultaneous requirement $\mu_1 = 0 = \mu_2$.

At $O(\eta^2)$ the diffusion equations yield the coefficients u_{12z}, u_{22z}, v_{12z}, and v_{22z} while the different Fourier components of boundary conditions (25) and (26) give the remaining coefficients in the expansions for u and v. Boundary condition (24) yields

$$\hat{\tau}_1 \partial_{T_1} z_{11} = \hat{\mu}_1 z_{12} + (\hat{\mu}_{1,\xi}\xi_1 + \hat{\mu}_{1,\gamma}\gamma_1 + \hat{\mu}_{1,q} q_1) z_{11} + \hat{c}_1 z_{11} z_{21} \ , \tag{A8a}$$

$$\hat{\tau}_2 \partial_{T_1} z_{21} = \hat{\mu}_2 z_{22} + (\hat{\mu}_{2,\xi}\xi_1 + \hat{\mu}_{2,\gamma}\gamma_1 + \hat{\mu}_{2,q} q_1) z_{21} + \hat{c}_2 z_{11}^2 \ . \tag{A8b}$$

Here $\hat{\mu}_{i,\xi}$ denotes the derivative of $\hat{\mu}_i$ with respect to ξ and similarly for $\hat{\mu}_{i,\gamma}$ and $\hat{\mu}_{i,q}$. These terms give therefore the first-order corrections to the zeroth-order growth rates [which vanish due to (A5)]. The quadratic coefficients are given by

$$2\hat{c}_1 = 2(\lambda_1+2)(\lambda_2+2)(k-1)/k - 2(\alpha k - 1)q_0^2(\xi_0 + \gamma_0 q_0^2) + [2(\alpha k - 1)q_0^2 - k(\alpha\Lambda_1 + 2)\Lambda_2 + (\lambda_1+2)\lambda_2](\xi_0 + 4\gamma_0 q_0^2) \ , \tag{A9}$$

$$2\hat{c}_2 = [2(\lambda_1+1)(\lambda_2+2) - 4q_0^2](k-1)/k + (\xi_0 + \gamma_0 q_0^2)[2q_0^2(\alpha k - 1) - \Lambda_1(\Lambda_2\alpha + 2)k + \lambda_1(\lambda_2+2)] \ . \tag{A10}$$

Similarly, proceeding to third order one obtains the coefficients u_{13z}, $u_{13zz}\ldots$ from the diffusion equations and the remaining coefficients from boundary conditions (25) and (26). Again the dynamical equations are obtained from boundary condition (24),

$$\begin{aligned}\hat{\tau}_1 \partial_{T_2} z_{11} + \hat{\tau}_1 \partial_{T_1} z_{12} + (\hat{\tau}_{1,\xi}\xi_1 + \cdots)\partial_{T_1} z_{11} &= \hat{\mu}_1 z_{13} + (\hat{\mu}_{1,\xi}\xi_1 + \hat{\mu}_{1,\gamma}\gamma_1 + \hat{\mu}_{1,q} q_1) z_{12} + (\hat{\mu}_{1,\xi q}\xi_1 q_1 + \hat{\mu}_{1,\gamma q}\gamma_1 q_1 + \hat{\mu}_{1,qq} q_1^2) z_{11} \\ &+ \hat{c}_1 z_{12} z_{21} + \hat{c}_1 z_{11} z_{22} + z_{11} z_{21}(\hat{c}_{1\xi}\xi_1 + \hat{c}_{1\gamma}\gamma_1 + \cdots) + \hat{f}_1 \partial_{T_1}^2 z_{11} + \hat{g}_1 z_{11} \partial_{T_1} z_{21} \\ &+ \hat{g}_2 z_{21} \partial_{T_1} z_{11} + z_{11}(\hat{a}_1 z_{11}^2 + \hat{b}_1 z_{21}^2)\end{aligned} \tag{A11}$$

and a similar equation for $\partial_{T_2} z_{21}$. Again $\hat{\tau}_{1,\xi}$ denotes the ξ derivative of $\hat{\tau}_1$, etc. The expressions for the third-order coefficients $\hat{a}_i$ and $\hat{b}_i$ are too lengthy to display here [29]. The amplitude equations in the form (30) are now obtained by reconstitution [30]. To this end η times (A5) + η^2 times (A8) + η^3 times (A11) are added up. The resulting equations can be simplified considerably by noting that all the coefficients involving ξ_1, γ_1, and q_1 represent corrections to the corresponding values evaluated at the codimension-2 point. Thus their contributions can be summed up by evaluating the coefficients for the parameter values γ, ξ, and q in question, avoiding the expansion (A3),

$$\bar{\tau}_1 = \hat{\tau}_1 + \hat{\tau}_{1,\xi}\xi_1 + \hat{\tau}_{1,\gamma}\gamma_1 + \cdots \tag{A12}$$

and

$$\bar{\mu}_1(q,\gamma,\xi) = \bar{\tau}_1^{-1}(\hat{\mu}_1 + \hat{\mu}_{1,\xi}\xi_1 + \hat{\mu}_{1,\gamma}\gamma_1 + \hat{\mu}_{1,q} q_1 + \hat{\mu}_{1,\xi q}\xi_1 q_1 + \cdots) \ , \tag{A13}$$

$$\bar{c}_1(q,\gamma,\xi) = \bar{\tau}_1^{-1}(\hat{c}_1 + \hat{c}_{1,\xi}\xi_1 + \hat{c}_{1,\gamma}\gamma_1 + \hat{c}_{1,q} q_1 + \hat{c}_{1,\xi q}\xi_1 q_1 + \cdots) \ , \tag{A14}$$

and similarly for the other coefficients. At the same time one can introduce new amplitudes

$$z_1 = \eta z_{11} + \eta^2 z_{12} + \cdots \ , \tag{A15a}$$

$$z_2 = \eta z_{21} + \eta^2 z_{22} + \cdots \ , \tag{A15b}$$

which are the full amplitudes of the respective Fourier modes of the interface deflection. To go back to the translationally invariant system, i.e., to complex amplitudes, one notes that any solution to the restricted equations with real amplitudes must also solve the full complex equations. Using the definition $Z_1 e^{iqx} + \text{c.c.} = z_1 \cos qx$ and going back to the unscaled time variable one then obtains

$$\partial_t Z_1=\bar{\mu}_1 Z_1+\bar{c}_1 Z_1^* Z_2+\bar{f}_1\partial_t^2 Z_1+\bar{g}_1 Z_1^*\partial_t Z_2 +\bar{g}_2 Z_2\partial_t Z_1^*+Z_1(\tilde{a}_1|Z_1|^2+\tilde{b}_1|Z_2|^2)\ , \tag{A16a}$$

$$\partial_t Z_2=\bar{\mu}_2 Z_2+\bar{c}_2 Z_1^2+\bar{f}_2\partial_t^2 Z_2+\bar{g}_3 Z_1\partial_t Z_1 +Z_2(\tilde{a}_2|Z_1|^2+\tilde{b}_2|Z_2|^2)\ , \tag{A16b}$$

with

$$\tilde{c}_1=2\bar{c}_1,\quad \tilde{c}_2=2\bar{c}_2\ , \tag{A17}$$

$$\tilde{g}_1=2\bar{g}_1,\quad \tilde{g}_2=2\bar{g}_2,\quad \tilde{g}_3=2\bar{g}_3\ , \tag{A18}$$

$$\tilde{a}_i=4\bar{a}_i,\quad \tilde{b}_i=4\bar{b}_i\ . \tag{A19}$$

These equations could now be analyzed instead of the amplitude equations (30). Note that the second-order time derivatives arise since the linear dispersion relation is nonlinear in the growth rates μ_i, in particular, since λ_i and Λ_i depend on μ_i [Eqs. (A4) are valid only on the neutral curve]. Therefore the expansion leads to time derivatives of arbitrarily high order. To make use of the results of previous analyses [24,23,25] it is useful to eliminate all higher-order time-derivative terms recursively,

$$\partial_t^2 Z_1=\bar{\mu}_1^2 Z_1+\tilde{c}_1(2\bar{\mu}_1+\bar{\mu}_2)Z_1^* Z_2+\tilde{c}_1\tilde{c}_2 Z_1|Z_1|^2 +\tilde{c}_1^2 Z_1|Z_1|^2\ , \tag{A20a}$$

$$\partial_t^2 Z_2=\bar{\mu}_2^2 Z_2+\tilde{c}_2(2\bar{\mu}_1+\bar{\mu}_2)Z_1^2+2\tilde{c}_1\tilde{c}_2 Z_2|Z_1|^2\ , \tag{A20b}$$

$$Z_1^*\partial_t Z_2=\bar{\mu}_2 Z_1^* Z_2+\tilde{c}_2 Z_1|Z_1|^2\ , \tag{A20c}$$

$$Z_2\partial_t Z_1^*=\bar{\mu}_1 Z_1^* Z_2+\tilde{c}_1 Z_1|Z_2|^2\ , \tag{A20d}$$

$$Z_1\partial_t Z_1=\bar{\mu}_1 Z_1^2+\tilde{c}_1 Z_2|Z_1|^2\ . \tag{A20e}$$

Thus one finally obtains

$$\dot{Z}_1=\mu_1 Z_1+c_1 Z_1^* Z_2+a_1 Z_1|Z_1|^2+b_1 Z_1|Z_2|^2\ , \tag{A21a}$$

$$\dot{Z}_2=\mu_2 Z_2+c_2 Z_1^2+a_2 Z_2|Z_1|^2+b_2 Z_2|Z_2|^2\ , \tag{A21b}$$

with

$$\mu_i=\bar{\mu}_i+\bar{f}_i\bar{\mu}_i^2\ , \tag{A22a}$$

$$c_1=\tilde{c}_1+\bar{f}_1\tilde{c}_1(2\bar{\mu}_1+\bar{\mu}_2)+\bar{g}_1\bar{\mu}_2+\bar{g}_2\bar{\mu}_1\ , \tag{A22b}$$

$$c_2=\tilde{c}_2+\bar{f}_2\tilde{c}_2(2\bar{\mu}_1+\bar{\mu}_2)+\bar{g}_3\bar{\mu}_1\ , \tag{A22c}$$

$$a_1=\tilde{a}_1+\bar{f}_1\tilde{c}_1\tilde{c}_2+\bar{g}_1\tilde{c}_2\ , \tag{A22d}$$

$$a_2=\tilde{a}_1+2\bar{f}_2\tilde{c}_1\tilde{c}_2+\bar{g}_3\tilde{c}_1\ , \tag{A22e}$$

$$b_1=\tilde{b}_1+\bar{f}_1\tilde{c}_1^2+\bar{g}_2\tilde{c}_1\ , \tag{A22f}$$

$$b_2=\tilde{b}_2\ . \tag{A22g}$$

In the comparison with the numerical solutions these equations are used with the coefficients evaluated at the parameter values in question. As the reconstitution shows, the terms z_{12}, z_{22}, etc., as well as ξ_1,γ_1,q_1 need not be kept to obtain the final equations. This simplifies the calculation noticeably.

---

*Present address: Laboratoire de Physique Statistique, Ecole Normale Supérieure, 24 rue Lhomond, F-75231 Paris CEDEX 05, France.

[1] A. Simon, J. Bechloefer, and A. Libchaber, Phys. Rev. Lett. **61**, 2574 (1988).
[2] J.-M. Flesselles, A. Simon, and A. Libchaber, Adv. Phys. **40**, 1 (1991).
[3] M. Rabaud, S. Michalland, and Y. Couder, Phys. Rev. Lett. **64**, 184 (1990).
[4] G. Faivre, S. de Cheveigné, C. Guthmann, and P. Kurowski, Europhys. Lett. **9**, 779 (1989).
[5] G. Ahlers, in *Lectures in the Sciences of Complexity,* edited by D. L. Stein (Addison-Wesley, Reading, MA, 1989), Vol. I.
[6] F. Daviaud, M. Dubois, and P. Berge, Europhys. Lett. **9**, 411 (1989).
[7] P. Coullet and G. Iooss, Phys. Rev. Lett. **64**, 866 (1990).
[8] For a review see, e.g., J. Langer, in *Chance and Matter,* edited by J. Soulette, J. Vannimenus, and R. Stora (North-Holland, Amsterdam, 1987).
[9] D. A. Kessler, J. Koplik, and H. Levine, Adv. Phys. **37**, 255 (1988).
[10] P. Coullet, R. E. Goldstein, and G. H. Gunaratne, Phys. Rev. Lett. **64**, 866 (1990).
[11] R. E. Goldstein, G. H. Gunaratne, and L. Gil, Phys. Rev. A **41**, 5731 (1990).
[12] P. Haug, Phys. Rev. A **40**, 7253 (1989); Nucl. Phys. B Suppl. **5A**, 296 (1988).
[13] D. A. Kessler and H. Levine, Phys. Rev. A **39**, 3041 (1989).
[14] H. Levine and W.-J. Rappel, Phys. Rev. A **42**, 7475 (1991).
[15] D. A. Kessler and H. Levine, Phys. Rev. A **41**, 3197 (1990).
[16] H. Levine, W.-J. Rappel, and H. Riecke, Phys. Rev. A **43**, 1122 (1991).
[17] B. Caroli, C. Caroli, and B. Roulet, J. Phys. (Paris) **43**, 1767 (1982).
[18] D. J. Wollkind, D. B. Oulton, and R. Sriranganthan, J. Phys. (Paris) **45**, 505 (1984).
[19] S. de Cheveigné, C. Guthmann, and M. Lebrun, J. Phys. (Paris) **47**, 2095 (1986).
[20] For earlier work on mode interactions see L. H. Ungar and R. A. Brown, Phys. Rev. B **29**, 1367 (1984); G. Dee and R. Mathur, *ibid.* **27**, 7073 (1983).
[21] H. Riecke and H.-G. Paap, Phys. Rev. A **33**, 547 (1986).
[22] H.-G. Paap and H. Riecke, Phys. Rev. A **41**, 1943 (1990).
[23] C. A. Jones, and M. R. E. Proctor, Phys. Lett. A **121**, 224 (1987); M. R. E. Proctor and C. A. Jones, J. Fluid Mech. **188**, 301 (1988).
[24] G. Dangelmayer, Dyn. Stab. Syst. **1**, 159 (1986).
[25] D. Armbruster, J. Guckenheimer, and P. Holmes, Physica D **29**, 257 (1988); SIAM (Soc. Ind. Appl. Math.) J. Appl. Math. **49**, 676 (1989).
[26] W.-J. Rappel (unpublished).
[27] In the supercritical case the TW's are in general unstable close to onset. Recently, it has therefore been speculated

that this may be an alternative explanation for the solitary solutions [S. Fauve, S. Douady, and O. Thual, J. Phys. (Paris) II **1**, 311 (1991)].
[28] H. Riecke and H.-G. Paap (unpublished).
[29] The analytical expressions for all of the coefficients can be obtained from the authors upon request.
[30] A. J. Roberts, SIAM (Soc. Ind. Appl. Math.) J. Math. Anal. **16**, 1243 (1985).